Published in final edited form as:

Magn Reson Med. 2018 March ; 79(3): 1420–1428. doi:10.1002/mrm.26800.

Establishing the Overlap of IONP Quantification with Echo and Echoless MR Relaxation Mapping

Hattie L. Ring[1], **Jinjin Zhang**[1], **Nathan D. Klein**[2], **Lynn E. Eberly**[3], **Christy L. Haynes**[2], and **Michael Garwood**[1]

[1]Center for Magnetic Resonance Research, Department of Radiology, University of Minnesota, Minneapolis, USA

[2]Department of Chemistry, University of Minnesota, Minneapolis, USA

[3]Division of Biostatistics, University of Minnesota, Minneapolis, USA

Abstract

Purpose—Iron oxide nanoparticles (IONPs) have shown tremendous utility for enhancing image contrast and delivering targeted therapies. Quantification of IONPs has been demonstrated at low concentrations with gradient echo (GRE) and spin echo (SE), and at high concentrations with echoless sequences such as swept imaging with Fourier transform (SWIFT). This work examines the overlap of IONP quantification with GRE, SE and SWIFT.

Methods—The limit of quantification (LOQ) of GRE, SE, inversion recovery (IR) GRE, and SWIFT sequences was assessed using IONPs at a concentration range of 0.02 to 89.29 mM suspended in 1% agarose. Empirically derived LOQs were compared with International Union of Pure and Applied Chemistry (IUPAC) definitions. Both commercial and experimental IONPs were used.

Results—All three IONPs assessed demonstrated an overlap of concentration quantification with GRE, SE, and SWIFT sequences. The largest dynamic range observed was 0.004 to 35.7 mM with Feraheme.

Conclusion—The metrics established allow upper and lower quantitative limitations to be estimated given the relaxivity characteristics of the IONP and the concentration range of the material to be assessed. The methods outlined in this paper are applicable to any pulse sequence, IONP formulation, and field strength.

Keywords

Iron oxide nanoparticle; SWIFT; T_1, T_2, and T_2* quantitation; MRI

Corresponding Author: Michael Garwood, 1-211B, Center for Magnetic Resonance Research, University of Minnesota, 2021 Sixth Street SE, Minneapolis, MN 55455.

Introduction

Iron oxide nanoparticles (IONPs) are finding increased utility in clinical and pre-clinical settings for diagnostic and therapeutic purposes (1,2). IONP-based contrast agents used in MRI applications, such as FDA-approved Resovist and Feridex, typically produce hypo-intense signal (negative contrast) when imaged with gradient-echo (GRE) and spin-echo (SE) sequences (1,3,4). While low concentrations of IONPs can often be quantified with GRE and SE sequences, quantification of high IONP concentrations is not possible with these methods due to the strong negative contrast produced. Yet, the ability to quantify IONPs over a broad concentration range is desirable for many emerging applications of IONPs, such as cell targeting (5–9), drug delivery (2,10), magnetic fluid hyperthermia treatment of cancers (11–13), neuromodulation (14), and nanowarming of cryopreserved tissues (15).

GRE and SE sequences are sensitive to IONPs (< 0.18 mM) due to their finite minimum echo time (typically TE > 1 ms) and the short T_2 and T_2* of spins in the presence of IONPs (16). At high IONP concentrations, T_2 and T_2* values become too short to enable accurate IONP quantification. Recently, several echoless pulse sequences have been developed to preserve signal from spins with ultra-short T_2 or T_2*, for example ultra-short echo time (UTE), zero echo time (ZTE), swept imaging with Fourier transformation (SWIFT), and pointwise encoding time reduction with radial acquisition (PETRA) (17–22). In this work, a T_1-weighted SWIFT sequence (23) is compared with GRE and SE sequences for quantifying IONPs. SWIFT exploits frequency-modulated excitation and a simultaneous acquisition strategy to preserve signals arising from spins having almost any R_2 (= $1/T_2$) (6,19,23–27). This sequence has been demonstrated to measure high concentrations of IONPs both in agarose and in vivo (23,28). In vivo quantification of IONPs in various organs was shown to be possible at concentrations as high as 61 mM Fe (23,28).

The quantification of IONPs using MRI has been demonstrated at both low and high IONP concentrations (23,28,29). Thus far, the overlap of the quantifiable ranges provided by GRE and SE, and echoless sequences like SWIFT, has not been explored. Herein, the dynamic range of IONP quantification with GRE, SE, inversion-recovery gradient echo (IR-GRE), and SWIFT is assessed to establish metrics for defining the upper and lower quantification limits.

Methods

Experimental Nanoparticle Synthesis and Characterization

Functionalized mesoporous silica-coated IONPs (msIONPs) were produced with superparamagnetic iron oxide cores (EMG-308, Ferrotec USA) following a previously described protocol to synthesize the mesoporous silica shell with a polyethylene glycol and trichloromethylsilane coating (30). Iron content of the msIONPs was verified using inductively coupled plasma optical emission spectrometry.

Commercial Nanoparticle

Two commercial nanoparticles were compared: an IONP used for magnetic fluid hyperthermia applications, EMG-308 (Ferrotec, USA), and an FDA-approved IONP used for anemia treatment which has also generated interest as an MRI contrast agent, Feraheme (Amag Pharmaceuticals, Waltham, MA) (31,32).

Phantom Preparation

IONPs were suspended in 1% agarose in 6 mm × 50 mm culture tubes. The lower limit of quantitation (LOQ) was assessed with msIONPs at concentrations ranging from 0.02 to 1.79 mM. The full LOQ range was assessed at concentrations ranging from 0.02 to 35.71 mM. Finally, the upper LOQ was assessed with the commercial particles from 17.86 to 89.29 mM. A control (1% agarose only) sample was included with all measurements. Up to nine samples were held in place using a teflon holder which was inserted into a 50 mL polyethylene terephthalate (PET) centrifuge tube filled with 0.9% saline.

Image Acquisition

MR imaging was performed over several imaging sessions. All MR images were acquired in a 9.4-T 31-cm bore magnet (Magnex Scientific, Yarnton, UK) interfaced to a research console (Varian, Palo Alto, CA). All images were acquired with a volume transmit/receive coil having an inner diameter of 3 cm (Varian, Palo Alto, CA).

The goal in this work was to assess the overlap between R_1-, R_2-, and R_2*-based IONP quantifications. SWIFT, GRE, SE, and IR-GRE were used to assess that overlap. SWIFT was selected based on recent *in vivo* studies demonstrating an R_1 and IONP concentration calibration at high IONP concentrations (≤ 61 mM) (28). IR-GRE provided a short-TE R_1 mapping sequence for comparison with the echoless R_1 mapping provided by SWIFT. GRE and SE were selected as standard pulse sequences for R_2* and R_2 measurement, respectively. Sequence parameter settings were not selected to optimize over the entire IONP concentration range. Instead, for conventional sequences (GRE, SE, and IR-GRE) TR and TE values were set within practical limits to achieve optimal sensitivity for high IONP concentrations, whereas, the parameter settings for SWIFT were based on previous studies which had a concentration range that would overlap with GRE, SE, and IR-GRE sequences (16,28). Furthermore, since the focus of this study was to ascertain the overlap of the quantifiable IONP ranges achievable with these techniques and not a direct comparison of imaging metrics, the receiver gain used for each sequence was selected to obtain the best image and not to match the signal to noise ratio between sequences.

GRE, SE, and IR-GRE acquisitions were used to produce two-dimensional (2D) maps of R_2* (=1/T_2*), R_2 (=1/T_2), and R_1 (=1/T_1), respectively. Each image was acquired with bandwidth (BW) = 50 kHz, acquisition time = 2.56 ms, slice thickness = 5 mm, and resolution = 417 × 417 μm^2. GRE images were acquired with TR = 1.2 s and flip angle = 20°. TE was arrayed across 16 points spaced logarithmically between 3 and 400 ms. SE images were acquired with TR = 2.4 s. TE was arrayed across 16 points spaced logarithmically between 12 and 800 ms. IR-GRE images were acquired with TR = 21000 ms, TE = 5 ms, and flip angle = 10°. TI was arrayed across 8 points spaced exponentially

between 12 ms and 8 s. All 2D images were reconstructed using VnmrJ version 3.2. SWIFT was used as a representative T_2- and T_2*-insensitive pulse sequence. The SWIFT 3D R_1 map was acquired using a Look-Locker method with a multi-band (MB) SWIFT sequence for image readout using flip angle = 1°, acquisition delay ≈ 2 μs, BW = 384 kHz, TR = 1.2 ms, gaps = 2, voxel resolution = 194 × 194 × 1172 μm^3, and total acquisition time around 7 min (23,33). The field-of view (FOV) was 50 × 50 × 150 mm^3 with image matrix size = 128 × 128 × 128 × 64 (x,y,z,t). Two different MB-SWIFT settings, which impact the time points acquired, were also adjusted (N_{spiral} = 128 and 32 and N_v = 1024 and 4096, respectively). The N_v = 1024 setting had 64 time points spaced linearly from 12.7 to 1152 ms. The N_v = 4096 setting had 64 time points spaced linearly from 39.8 to 4596 ms. MB-SWIFT images were reconstructed using an in-house program written in MATLAB (2012b) (33).

Measurements determining the lower LOQ were performed with msIONPs only and required triplicate images acquired within the same session repeated across three separate sessions. This resulted in 9 images total. Measurements used to determine the relaxivity values (r_1, r_2, and r_2*) for the commercially available IONPs were derived from a single image.

Relaxation Determination

For each voxel, the time points along the recovery or decay curve were fit using a three-parameter mono-exponential fit. The use of the three-parameter fit is most critical for high IONP concentrations where full saturation or inversion recovery may not be achieved and the residual magnetization should be removed from the fit (23). A specific amplitude could not be assumed for this fit; therefore, broad boundaries were selected. These broad boundaries allow both an exponential decay or growth fit based on the pulse sequence evaluated. More details about this fit and the impact of boundary selection on the R_x are discussed in Supplemental Information. The relaxivity measurements were determined with least-squares fitting. The region of interest (ROI) assessed for each tube was a cuboid with dimensions: 2.05 × 2.05 × 5 mm. For GRE, SE, and IR-GRE, this resulted from drawing a 6 × 6 voxel square in the center of each tube for the single slice acquired. For SWIFT, this was acquired by drawing a 12 × 12 voxel square within the center of each tube across 4 slices.

Error Sources

Three error sources were compared for the determination of the LOQ. The three sources of error investigated are: (1) the standard error of the exponential fit (“Fit”), (2) the standard deviation between measurements within the same imaging session (“Within Session”), (3) the standard deviation between average measurements made during different imaging sessions (“Between Sessions”). To be comparable, each of these variations was re-scaled as a percentage of the mean R_x measured. For all measurements, the observed dynamic range (linear region of calibration curve) was used to define the upper and lower LOQ. More discussion on the metrics used to define the lower and upper LOQ are given in the Results and Discussion. A fit standard error above 5% was observed to indicate a measurement was above the upper LOQ for GRE, SE, and IR-GRE sequences and therefore a bad quantitative measurement. Samples with a low IONP concentration were observed to be below this

threshold. The lower LOQ was assessed after the largest source of error was defined as the standard deviation of the blank.

Lower Limit Assessment

There are three different terms which are often utilized to describe quantification capabilities: critical limit (x_C), limit of detection (x_D), and limit of quantification (x_Q) (34). For this work, we use the nomenclature and equations from the 1995 IUPAC standard which allowed a direct comparison of x_C, x_D, and x_Q (35). The critical limit (x_C) indicates the lowest possible amount of analyte that could be measured with a detector (Table 1, Eq. 1). This measurement has a 5% statistical overlap with the blank measurement and therefore has the possibility of false positive results. The detection limit (x_D) indicates the lowest possible amount of analyte where overlap with the blank is negligible (Table 1, Eq. 2). Both x_C and x_D account for the statistical overlap with the blank, number of standard solutions measured for the calibration, and the range of concentrations measured for the calibration. The quantification limit (x_Q) indicates the lowest possible amount of analyte that can be quantified separately from the blank (Table 1, Eq. 3). This equation guarantees no overlap with the blank by ensuring a distance from the blank that is an order of magnitude larger than the standard deviation of the background matrix (i.e. blank). The lower LOQ defined by x_C, x_D, and x_Q were compared with the empirical quantification limit, which was defined from the results of a one-way ANOVA with Dunnett comparisons to the control. Statistical analysis was performed using Graphpad Prism version 6.02 (GraphPad Software, La Jolla California USA).

Upper Limit Assessment

The upper LOQ is often defined as the “loss of linearity” within the calibration curve, which is dependent on the detection method (36). For MR quantification, the R_x values are defined from the exponential curve fit to the change in signal over time. As higher IONP concentrations are measured, a smaller signal change occurs, resulting in a less robust exponential fit. The impact of a less robust fit was observed to be different between echo and echoless sequences. For echo sequences (GRE, SE, and GRE-IR), a less robust exponential fit was observed with a drastic increase in the exponential fit standard error (see Supporting Figure S1). Measurements within the dynamic range were observed to be < 0.1% while those above the dynamic range had a standard error > 100%, of the R_x value. SWIFT demonstrated a low exponential fit standard error, despite the measurements obviously being beyond the dynamic range. However, as higher IONP concentrations are achieved for SWIFT, it becomes more difficult to fully saturate the signal, changing the exponential fit amplitude (23). The amplitude of the exponential fit and the R_1 value were observed to change based on the boundary conditions given for the exponential fit, indicating the fits were not robust (see Supporting Figure S2). More details are given on this determination within the supplemental information.

Results

Initial studies are performed with msIONPs, because their R_1 correlation with IONP concentration has been demonstrated in vivo (28). The relaxivity maps of msIONPs at a

broad concentration range (0.02 to 35.71 mM) demonstrate the upper limits of detection for traditional pulse sequences (Figure 1). Upper limits of detection are 1.79, 0.89, and 1.79 mM for GRE, SE, and IR-GRE, respectively. For these pulse sequences the upper limit of detection is equivalent to the quantifiable upper limit. With samples containing IONP concentrations above this limit, signal voids in the images limit the ability to obtain adequate exponential decay fits for determining relaxation time.

The R_1 values acquired with IR-GRE and SWIFT methods are compared. These values are the same at low IONP concentrations, but a deviation between these two methods is observed msIONP concentrations >1.79 mM. A comparison between these measurements is demonstrated with a Bland-Altman plot (Figure 2), for which the x-axis indicates the mean R_1 and the y-axis indicates the difference between the R_1 values.

The different sources of error in the quantification of IONP concentration are compared with the msIONP dataset (Figure 3). The average percent error across the entire detectable range is plotted with the standard deviation within the detectable range. The error between imaging sessions was determined to be the dominant source of error and is therefore used as the standard deviation of the blank for the calculation of x_C, x_D, and x_Q. The calculated lower LOQ defined by x_Q is found to most directly match with the empirically derived results (Table 2). For each of the sequences, the calculated limit of quantitation is determined to be just below the empirically defined measurement (Figure 4).

To act as a comparison with previously published work, two different view settings are investigated with the SWIFT sequence (28). The change in the view settings adjusts the sample range along the recovery curve (Figures 5a and b). The number of view orders (N_v) 1024 and 4096 are compared; in this comparison, the number of view sets (N_{vs}) are adjusted to 512 and 128 to maintain the same scan time. The impact of the sample range on the exponential fit standard error can be observed between the standard fit error. Maps are shown in Figures 5c and d. The best selection of view settings as a function of IONP concentration is determined by comparing the standard fit error. A lower standard error indicates a better fit and therefore is a more accurate measurement. The lower view order setting (N_v = 1024) is optimal at higher IONP concentrations, more specifically above 8.93 mM, whereas the higher view order setting performs better at low IONP concentrations (N_v = 4096).

The r_1, r_2, and r_2* of each IONP is listed in Table 3 with the approximated lower and upper limit of quantification. Higher IONP concentrations (up to 89.29 mM) are explored using only the commercially available IONPs (Figure 6) because it was technically challenging to achieve these high concentrations with synthesized msIONPs. The upper LOQ is observed at concentrations above 35.71 mM for both commercial IONPs. A discrepancy is observed between measurements made over a broad concentration range (0 – 89.29 mM) and only the high concentration range (44.64 – 178.57 mM) at 53.57 and 89.29 mM. This discrepancy is attributed to these measurements being above the upper LOQ for Feraheme and EMG-308.

Discussion

Several non-invasive imaging methods have been applied to quantify IONPs. X-ray computed tomography (CT) is used clinically for hyperthermia cancer therapeutics in Europe, but is only useful for high concentrations (> 89mM) (16). Magnetic Particle Imaging (MPI) is a very promising tracer-based imaging method which directly detects IONPs. MPI has been demonstrated at concentrations ranging from 150 nm to 189 mM (37,38). This range is beyond the 6 μM lower LOQ shown with Feraheme and the 53 mM upper LOQ shown with Feraheme. Currently, only preclinical MPI scanners are available, but recent studies have shown great promise toward applications in traumatic brain injuries, magnetic fluid hyperthermia, liver visualization, kinetics tracing of IONPs, and assessing IONP biodistribution (37). Quantitative susceptibility mapping determines the magnetic susceptibility of a material through phase information with GRE (39). Unlike R_2 and R_2* mapping, QSM is not susceptible to blooming artifacts, therefore it is considered more accurate and has potential to extend past the quantification limitations for R_2* (40). IONP quantification has been demonstrated for cell targeting and IONP accumulation and distribution in vivo (40–43). In contrast, R_1, R_2, and R_2* maps are already applied clinically and have the capability to non-invasively quantify IONPs at much lower concentrations than CT.

Quantification of endogenous iron with magnetic resonance is already an established clinical technique (44–46). These protocols, which use SE and GRE methods, have been expanded to demonstrate IONP quantification within in vivo studies (5,47). In both cases, the limitation of these pulse sequences is caused by the minimum achievable echo time (TE) and the fast T_2 and T_2* decay caused by the presence of iron and iron-oxide. Several recently developed sequences have zero or negligible acquisition delay, allowing for the detection of signals with rapid T_2 and T_2* relaxation and acquiring contrast through T_1 relaxation (19,22,23,33,48–51). These methods have been able to demonstrate the quantification of IONPs as high as 54 mM in 1% agar, 61 mM in organs, and 2.9 mM in blood (23,49,50). All of these works have focused on the extension of the IONP quantification range, whereas herein, we focus on the IONP concentration overlap between conventional MRI methods, such as GRE, SE, and IR-GRE, and T_2-insensitive pulse sequences, such as SWIFT. This allows for future studies to be designed based on the relevant IONPs available and the desired concentration range of quantification.

The main goal of this study was to assess the quantitative overlap between an echoless sequence (SWIFT) and conventional echo pulse sequences (GRE, SE, and IR-GRE). The settings for GRE, SE, and IR-GRE were chosen to increase the upper LOQ. More specifically, selecting a shorter TE increases the upper LOQ. In our case, the TE was constrained by the hardware. The lower TE for GRE compared to SE allowed GRE to quantify higher IONP concentrations. IR-GRE, a commonly used MRI technique for mapping T_1, becomes less reliable at high IONP concentrations due to impacts from short T_2*. Therefore, the upper LOQ for IR-GRE is also governed by the lowest achievable TE. There are alternative pulse sequences which are not hindered by hardware constraints and can reduce artifacts, thus providing a broader quantitative range, however, the purpose of

this work was not to focus on specific sequences under certain hardware limitations, but to instead describe a procedure that is applicable to any sequence or hardware constraints.

The parameter settings for SWIFT utilized previously known settings which have obtained R_1 values for samples ranging from 0 – 61 mM (28). It has been demonstrated that inversion recovery methods are problematic for fast relaxing samples, due to a diminished ability to achieve full inversion (23). The use of saturation rather than inversion preparation in SWIFT may explain why a lower limit of quantification was achieved with IR-GRE as compared with SWIFT. However, at the low IONP concentrations evaluated for the lower LOQ, the R_1 term is dominated by the intrinsic R_1 and the changes in IONP concentration are below the standard deviation observed between imaging sessions. Therefore a comparison of SWIFT using inversion recovery rather than saturation recovery is unlikely to have a large impact on the lower LOQ.

The two different SWIFT settings had a major impact on the IONP concentration that could be quantified. The observation that $N_v = 1024$ and $N_v = 4096$ settings worked best for higher and lower IONP concentration, respectively, follows the expectation from the time points acquired along the exponential fit. Based on the standard fit error maps, the $N_v = 1024$ setting is unsuitable to use for the very low IONP concentrations, 0.18 mM and below. On the other hand, the $N_v = 4096$ setting is capable of quantifying values for the entire range measured with the msIONPs. However, measurements at 35.71 mM and higher with commercial IONPs could not be quantified using the $N_v = 4096$ setting.

Clinical recommendations for the upper and lower boundaries of quantitative measurements using MRI relaxometry have previously been established. The lower bound for T_2 and T_2* was defined as two times the lowest TE (or TI, for T_1 measurements), while the upper bound was defined as one half the highest TE (or TI) (44). These definitions, which are based on pulse sequence settings, are defining the upper and lower limits based on the shortest and longest time points acquired along the exponential fit. Similar recommendations can be used for SWIFT, based on the acquired time points, as impacted by N_{spiral} and N_v. The boundaries described herein are instead empirically derived as described in the methods section. More specifically, it must be possible to distinguish the change in R_x caused by the amount of IONP present from the variations in the R_x of the intrinsic matrix. Several specific instances were discovered in which our empirical observation deviated from the clinical recommendations. Both SE and SWIFT demonstrated a smaller lower T_1 boundary (longer upper IONP concentration boundary) than the clinically recommended one. SWIFT and SE were able to measure T_1 and T_2 as short as 12.8 and 3.4 ms (corresponding to 35.71 and 1.79 mM in Table 3), despite the suggested 25.4 and 24 ms setting limits, respectively.

Within the defined quantitative range, it is no surprise that the dominant source of error was measured between different imaging sessions. With a chemically stable sample, it would be surprising to observe instabilities in the instrumentation that would cause large sources of variation. However, when the sample is completely removed from the magnet, small changes in sample placement, tuning, and shimming can have a more pronounced effect. This is most notable in GRE which is particularly susceptible to field inhomogeneities (52). The impact of inhomogeneity can be noted in GRE images of these samples in regions around the

highest IONP concentration. The inhomogeneity in the surrounding saline is likely caused by the high IONP concentration within the nearby sample. Furthermore, SE is a currently used clinical method for endogenous iron quantification, whereas GRE is still viewed as unreliable due to its sensitivity to the surrounding environment (45).

An important error source which was not explored in this work is the impact of working within complex biological environments. The surface coating on the IONP can have a major impact on the aggregation and accumulation within different cell types. For example, EMG-308 is known to aggregate within biological systems, whereas in in vitro studies an increased accumulation was observed and blooming artifacts were demonstrated with in vivo studies (30,53). In contrast, the application of a mesoporous silica coating (msIONPs) greatly improved stability and allowed for quantification within in vivo systems (28,30). Previous work with msIONPs demonstrated that accumulation of IONPs between different organs did impact the relaxivity (28). Furthermore, the IONP stability, which is dependent on the surface coating, should be understood for the time frame of the study (54). Degradation has been demonstrated for msIONPs within a week after intravenous injection (28). The impact of msIONP degradation after one week in vivo on relaxivity was negligible in some organs and a drastic changes in others (28). Finally, background produced by endogenous iron sources is likely to have a larger impact on the error than those outlined in this paper. T_2 and T_2* are known to be more susceptible to the change in endogenous iron (45). Additional studies have demonstrated a strong dependence between T_2 and the presence of ferritin, but a much lower response has been demonstrated with T_1 (55). Further studies are required to know the impact endogenous iron will have on the in vivo lower limit of IONP quantification using SWIFT. Furthermore, quantitative studies performed with pre-clinical and clinical studies will need to account for the endogenous iron variation between subjects when defining the lower LOQ.

The fact that the empirically derived limits match the IUPAC standard allows the lower LOQ to be estimated with the measured standard deviation of a dominant error source of a blank (1% agar, in our case) and the slope of the sample calibration. Therefore, the tedious repeated measurements only need to be performed once for each pulse sequence and background matrix, rather than for each sample. These same metrics could be applied to any IONP, but also for the quantification of any material with an impact on T_2, T_2*, and T_1.

Unlike GRE and SE, SWIFT's upper detection limit does not immediately decrease to zero signal. Therefore, the impact on the exponential fit amplitude was used to define the upper LOQ. At higher IONP concentrations, off-resonant effects create ringing artifacts in the image (23). This impact is best observed with commercial IONPs at concentrations above 17.86 mM, as shown in Figure 6. Interestingly, EMG-308 demonstrates a faster loss of contrast whereas Feraheme is more susceptible to the ringing artifact indicative of off-resonant effects. The loss of contrast with EMG-308 can be attributed to the higher r_1, r_2, and r_2* compared to Feraheme. Therefore, it is expected that EMG-308 would become susceptible to T_2 and T_2* dominant effects at lower concentrations than Feraheme. While these data indicate the upper limitation of IONP quantification with SWIFT is at 35.71 mM, it is important to note that there are many variations to the SWIFT sequence which could be

applied to expand the upper limit of IONP quantification, such as further adjustment to the N_{spiral} and N_v settings or the binning used in the reconstruction algorithm.

The current in vitro, ex vivo, and in vivo applications for non-invasive IONP quantification are varied, and therefore, as new IONPs are developed, evaluation of the quantitative range is essential to properly assess their use for a specific application. Currently, IONPs have been investigated for their utility in neuromodulation, cancer treatment based on magnetic fluid hyperthermia, cryopreservation, cell targeting, and drug delivery. Cell targeting requires detection of very low concentrations of IONPs and therefore an assessment of lower LOQ achievable with a given R_2- or R_2*-mapping sequence may be needed in some cases (5). On the other hand, hyperthermia and neuromodulation applications may require high concentrations of IONPs, therefore assessment with SWIFT, UTE, ZTE, and PETRA may be more applicable (14,16). Finally, assessing biodistribution for drug development applications requires a wide quantitative range, necessitating multiple pulse sequences to extend that range.

In this work, we focus only on the quantitative abilities of GRE, SE, IR-GRE, and SWIFT at one particular field strength, 9.4T. General conclusions about the limitations of these pulse sequences for measuring T_1, T_2, and T_2* are not rendered by this work. On the other hand, the methods outlined in this paper can be used as an assessment of quantitative overlap and are applicable to any pulse sequence, IONP formulation, and field strength. At 9.4T, an overlap between the GRE quantification and SWIFT quantification was established for all three IONPs assessed.

Conclusion

In summary, we have shown a way to estimate the upper and lower limits of IONP quantification with different relaxation mapping techniques. With this information, optimal pulse sequence selection is possible based on the relaxivity and concentration range of the material to be assessed. Furthermore, a large dynamic range for IONP quantification is possible when GRE and SWIFT measurements are combined.

Supplementary Material

Refer to Web version on PubMed Central for supplementary material.

Acknowledgments

This work was funded by: NIH P41 EB015894. ICP-OES was performed through University of Minnesota Research Analytical Lab.

References

1. Gupta AK, Gupta M. Synthesis and surface engineering of iron oxide nanoparticles for biomedical applications. Biomaterials. 2005; 26(18):3995–4021. [PubMed: 15626447]
2. Sun C, Lee JSH, Zhang M. Magnetic nanoparticles in MR imaging and drug delivery. Advanced Drug Delivery Reviews. 2008; 60(11):1252–1265. [PubMed: 18558452]
3. Wang Y-XJ. Superparamagnetic iron oxide based MRI contrast agents: Current status of clinical application. Quantitative Imaging in Medicine and Surgery. 2011; 1(1):35–40. [PubMed: 23256052]

4. Ros PR, Freeny PC, Harms SE, Seltzer SE, Davis PL, Chan TW, Stillman AE, Muroff LR, Runge VM, Nissenbaum MA. Hepatic MR imaging with ferumoxides: a multicenter clinical trial of the safety and efficacy in the detection of focal hepatic lesions. Radiology. 1995; 196(2):481–488. [PubMed: 7617864]
5. Kuhlpeter R, Dahnke H, Matuszewski L, Persigehl T, von Wallbrunn A, Allkemper T, Heindel WL, Schaeffter T, Bremer C. R2 and R2* Mapping for Sensing Cell-bound Superparamagnetic Nanoparticles: In Vitro and Murine in Vivo Testing. Radiology. 2007; 245(2):449–457. [PubMed: 17848680]
6. Zhou R, Idiyatullin D, Moeller S, Corum C, Zhang H, Qiao H, Zhong J, Garwood M. SWIFT detection of SPIO-labeled stem cells grafted in the myocardium. Magnetic Resonance in Medicine. 2010; 63(5):1154–1161. [PubMed: 20432286]
7. Billotey C, Wilhelm C, Devaud M, Bacri JC, Bittoun J, Gazeau F. Cell internalization of anionic maghemite nanoparticles: Quantitative effect on magnetic resonance imaging. Magnetic Resonance in Medicine. 2003; 49(4):646–654. [PubMed: 12652535]
8. Girard OM, Ramirez R, McCarty S, Mattrey RF. Toward absolute quantification of iron oxide nanoparticles as well as cell internalized fraction using multiparametric MRI. Contrast media & molecular imaging. 2012; 7(4):411–417. [PubMed: 22649047]
9. Weinstein JS, Varallyay CG, Dosa E, Gahramanov S, Hamilton B, Rooney WD, Muldoon LL, Neuwelt EA. Superparamagnetic iron oxide nanoparticles: diagnostic magnetic resonance imaging and potential therapeutic applications in neurooncology and central nervous system inflammatory pathologies, a review. Journal of Cerebral Blood Flow and Metabolism: Official Journal of the International Society of Cerebral Blood Flow and Metabolism. 2010; 30(1):15–35.
10. Sun C, Fang C, Stephen Z, Veiseh O, Hansen S, Lee D, Ellenbogen RG, Olson J, Zhang M. Tumor-targeted drug delivery and MRI contrast enhancement by chlorotoxin-conjugated iron oxide nanoparticles. Nanomedicine (London, England). 2008; 3(4):495–505.
11. Tate JA, Petryk AA, Giustini AJ, Hoopes PJ. In vivo biodistribution of iron oxide nanoparticles: an overview. Proceedings of SPIE. 2011; 7901:790117. [PubMed: 24478825]
12. Anselmo AC, Mitragotri S. A Review of Clinical Translation of Inorganic Nanoparticles. The AAPS Journal. 2015; 17(5):1041–1054. [PubMed: 25956384]
13. Dennis CL, Jackson AJ, Borchers JA, Hoopes PJ, Strawbridge R, Foreman AR, Van Lierop J, Grüttner C, Ivkov R. Nearly complete regression of tumors via collective behavior of magnetic nanoparticles in hyperthermia. Nanotechnology. 2009; 20(39):395103. [PubMed: 19726837]
14. Chen R, Romero G, Christiansen MG, Mohr A, Anikeeva P. Wireless magnetothermal deep brain stimulation. Science. 2015; 347(6229):1477. [PubMed: 25765068]
15. Manuchehrabadi N, Gao Z, Zhang J, Ring HL, Shao Q, Liu F, McDermott M, Fok A, Rabin Y, Brockbank KGM, Garwood M, Haynes CL, Bischof JC. Improved tissue cryopreservation using inductive heating of magnetic nanoparticles. Science Translational Medicine. 2017; 9(379)
16. Gneveckow U, Jordan A, Scholz R, Brüss V, Waldöfner N, Ricke J, Feussner A, Hildebrandt B, Rau B, Wust P. Description and characterization of the novel hyperthermia-and thermoablation-system MFH300F for clinical magnetic fluid hyperthermia. Medical physics. 2004; 31:1444–1444. [PubMed: 15259647]
17. Robson MD, Gatehouse PD, Bydder M, Bydder GM. Magnetic Resonance: An Introduction to Ultrashort TE (UTE) Imaging. Journal of Computer Assisted Tomography. 2003; 27(6)
18. Hafner S. Fast imaging in liquids and solids with the Back-projection Low Angle ShoT (BLAST) technique. Magnetic Resonance Imaging. 1994; 12(7):1047–1051. [PubMed: 7997092]
19. Idiyatullin D, Corum C, Park J-Y, Garwood M. Fast and Quiet MRI using a Swept Radiofrequency. Journal of Magnetic Resonance. 2006; 181(2):342–349. [PubMed: 16782371]
20. Grodzki DM, Jakob PM, Heismann B. Ultrashort echo time imaging using pointwise encoding time reduction with radial acquisition (PETRA). Magnetic Resonance in Medicine. 2012; 67(2): 510–518. [PubMed: 21721039]
21. Kobayashi N, Goerke U, Wang L, Ellermann J, Metzger GJ, Garwood M. Gradient-Modulated PETRA MRI. Tomography: a journal for imaging research. 2015; 1(2):85–90. [PubMed: 26771005]

22. Girard OM, Du J, Agemy L, Sugahara KN, Kotamraju VR, Ruoslahti E, Bydder GM, Mattrey RF. Optimization of Iron Oxide Nanoparticle Detection Using Ultrashort TE Pulse Sequences: Comparison of T(1), T(2)* and Synergistic T(1)-T(2)* Contrast Mechanisms. Magnetic resonance in medicine: official journal of the Society of Magnetic Resonance in Medicine/Society of Magnetic Resonance in Medicine. 2011; 65(6):1649–1660.
23. Zhang J, Chamberlain R, Etheridge M, Idiyatullin D, Corum C, Bischof J, Garwood M. Quantifying iron-oxide nanoparticles at high concentration based on longitudinal relaxation using a three-dimensional SWIFT look-locker sequence. Magnetic Resonance in Medicine. 2014; 71(6): 1982–1988. [PubMed: 24664527]
24. Garwood M. MRI of fast-relaxing spins. Journal of magnetic resonance. 2013:6–11. [PubMed: 23916990]
25. Garwood M, Chamberlain R, Etheridge M, Bischof J, et al. Capturing Signals from Ultrafast Relaxing Spins with SWIFT MRI and Its Usefulness for Molecular Imaging. 2011:T173–T173.
26. Idiyatullin D, Corum C, Moeller S, Garwood M. Gapped pulses for frequency-swept MRI. Journal of Magnetic Resonance. 2008; 193(2):267–273. [PubMed: 18554969]
27. Idiyatullin D, Suddarth S, Corum CA, Adriany G, Garwood M. Continuous SWIFT. Journal of Magnetic Resonance. 2012; 220:26–31. [PubMed: 22683578]
28. Zhang J, Ring HL, Hurley KR, Shao Q, Carlson CS, Idiyatullin D, Manuchehrabadi N, Hoopes PJ, Haynes CL, Bischof JC, Garwood M. Quantification and biodistribution of iron oxide nanoparticles in the primary clearance organs of mice using T1 contrast for heating. Magnetic Resonance in Medicine. 2016:n/a–n/a.
29. Corot C, Robert P, Idée J-M, Port M. Recent advances in iron oxide nanocrystal technology for medical imaging. Advanced Drug Delivery Reviews. 2006; 58(14):1471–1504. [PubMed: 17116343]
30. Hurley KR, Ring HL, Etheridge M, Zhang J, Gao Z, Shao Q, Klein ND, Szlag VM, Chung C, Reineke TM, Garwood M, Bischof JC, Haynes CL. Predictable Heating and Positive MRI Contrast from a Mesoporous Silica-Coated Iron Oxide Nanoparticle. Molecular Pharmaceutics. 2016
31. Bashir MR, Bhatti L, Marin D, Nelson RC. Emerging applications for ferumoxytol as a contrast agent in MRI. Journal of Magnetic Resonance Imaging. 2015; 41(4):884–898. [PubMed: 24974785]
32. Administration USFaD. , editor. Feraheme (ferumoxytol) Injection for Intravenous (IV) use. http://www.accessdata.fda.gov/drugsatfda_docs/label/2015/022180s011s013lbl.pdf2015
33. Idiyatullin D, Corum CA, Garwood M. Multi-Band-SWIFT. Journal of Magnetic Resonance. 2015; 251(0):19–25. [PubMed: 25557859]
34. Belter M, Sajnóg A, Barałkiewicz D. Over a century of detection and quantification capabilities in analytical chemistry – Historical overview and trends. Talanta. 2014; 129:606–616. [PubMed: 25127640]
35. Currie LA. Nomenclature in evaluation of analytical methods including detection and quantification capabilities (IUPAC Recommendations 1995). Pure and Applied Chemistry. 1995; 67:1699.
36. Skoog, DA., Holler, JF., Nieman, TA. Principles of Instrumental Analysis. North Miami Beach, FL: Murray Media; 1997.
37. Knopp T, Conolly SM, Buzug TM. Recent progress in magnetic particle imaging: from hardware to preclinical applications. Physics in Medicine and Biology. 2017; 62(9):E4. [PubMed: 28378712]
38. Hensley D, Tay ZW, Dhavalikar R, Zheng B, Goodwill P, Rinaldi C, Conolly S. Combining magnetic particle imaging and magnetic fluid hyperthermia in a theranostic platform. Physics in Medicine and Biology. 2017; 62(9):3483. [PubMed: 28032621]
39. Deistung A, Schweser F, Reichenbach JR. Overview of quantitative susceptibility mapping. NMR in Biomedicine. 2017; 30(4):e3569–n/a.
40. Klohs J, Deistung A, Ielacqua GD, Seuwen A, Kindler D, Schweser F, Vaas M, Kipar A, Reichenbach JR, Rudin M. Quantitative assessment of microvasculopathy in arcAβ mice with USPIO-enhanced gradient echo MRI. Journal of Cerebral Blood Flow & Metabolism. 2016; 36(9): 1614–1624. [PubMed: 26661253]

41. Wong R, Chen X, Wang Y, Hu X, Jin MM. Visualizing and Quantifying Acute Inflammation Using ICAM-1 Specific Nanoparticles and MRI Quantitative Susceptibility Mapping. Annals of Biomedical Engineering. 2012; 40(6):1328–1338. [PubMed: 22143599]
42. Di Corato R, Gazeau F, Le Visage C, Fayol D, Levitz P, Lux F, Letourneur D, Luciani N, Tillement O, Wilhelm C. High-Resolution Cellular MRI: Gadolinium and Iron Oxide Nanoparticles for in-Depth Dual-Cell Imaging of Engineered Tissue Constructs. ACS Nano. 2013; 7(9):7500–7512. [PubMed: 23924160]
43. Liu T, Spincemaille P, de Rochefort L, Wong R, Prince M, Wang Y. Unambiguous identification of superparamagnetic iron oxide particles through quantitative susceptibility mapping of the nonlinear response to magnetic fields. Magnetic Resonance Imaging. 2010; 28(9):1383–1389. [PubMed: 20688448]
44. Margaret Cheng H-L, Stikov N, Ghugre NR, Wright GA. Practical medical applications of quantitative MR relaxometry. Journal of Magnetic Resonance Imaging. 2012; 36(4):805–824. [PubMed: 22987758]
45. Hernando D, Levin YS, Sirlin CB, Reeder SB. Quantification of Liver Iron with MRI: State of the Art and Remaining Challenges. Journal of magnetic resonance imaging: JMRI. 2014; 40(5):1003–1021. [PubMed: 24585403]
46. Sirlin CB, Reeder SB. Magnetic Resonance Imaging Quantification of Liver Iron. Magnetic resonance imaging clinics of North America. 2010; 18(3):359, ix. [PubMed: 21094445]
47. Ma M, Chen H, Chen Y, Wang X, Chen F, Cui X, Shi J. Au capped magnetic core/mesoporous silica shell nanoparticles for combined photothermo-/chemo-therapy and multimodal imaging. Biomaterials. 2012; 33(3):989–998. [PubMed: 22027594]
48. Wang L, Corum CA, Idiyatullin D, Garwood M, Zhao Q. T(1) Estimation for Aqueous Iron Oxide Nanoparticle Suspensions Using a Variable Flip Angle SWIFT Sequence. Magnetic resonance in medicine: official journal of the Society of Magnetic Resonance in Medicine/Society of Magnetic Resonance in Medicine. 2013; 70(2)doi: 10.1002/mrm.24831
49. Zhang J, Ring HL, Hurley KR, Shao Q, Carlson CS, Idiyatullin D, Hoopes PJ, Haynes CL, Bischof JC, Garwood M. Quantification and Biodistribution of Iron Oxide Nanoparticles in the Primary Clearance Organs of Mice using Positive Contrast MRI for Heating. Mag Res Med. 2016 accepted.
50. Gharagouzloo CA, McMahon PN, Sridhar S. Quantitative contrast-enhanced MRI with superparamagnetic nanoparticles using ultrashort time-to-echo pulse sequences. Magnetic Resonance in Medicine. 2015; 74(2):431–441. [PubMed: 25168606]
51. Wang L, Zhong X, Qian W, Huang J, Cao Z, Yu Q, Lipowska M, Lin R, Wang A, Yang L, Mao H. Ultrashort Echo Time (UTE) imaging of receptor targeted magnetic iron oxide nanoparticles in mouse tumor models. Journal of Magnetic Resonance Imaging. 2014; 40(5):1071–1081. [PubMed: 25485347]
52. Chavhan GB, Babyn PS, Thomas B, Shroff MM, Haacke EM. Principles, Techniques, and Applications of T2*-based MR Imaging and Its Special Applications. Radiographics. 2009; 29(5): 1433–1449. [PubMed: 19755604]
53. Etheridge ML, Hurley KR, Zhang J, Jeon S, Ring HL, Hogan C, Haynes CL, Garwood M, Bischof JC. Accounting for biological aggregation in heating and imaging of magnetic nanoparticles. Technology. 2014; 02(03):214–228.
54. Szekeres M, Tóth IY, Illés E, Hajdú A, Zupkó I, Farkas K, Oszlánczi G, Tiszlavicz L, Tombácz E. Chemical and Colloidal Stability of Carboxylated Core-Shell Magnetite Nanoparticles Designed for Biomedical Applications. International Journal of Molecular Sciences. 2013; 14(7):14550–14574. [PubMed: 23857054]
55. Vymazal J, Brooks RA, Zak O, McRill C, Shen C, Chiro GD. T1 and T2 of Ferritin at Different Field Strengths: Effect on MRI. Magnetic Resonance in Medicine. 1992; 27(2):368–374. [PubMed: 1334206]

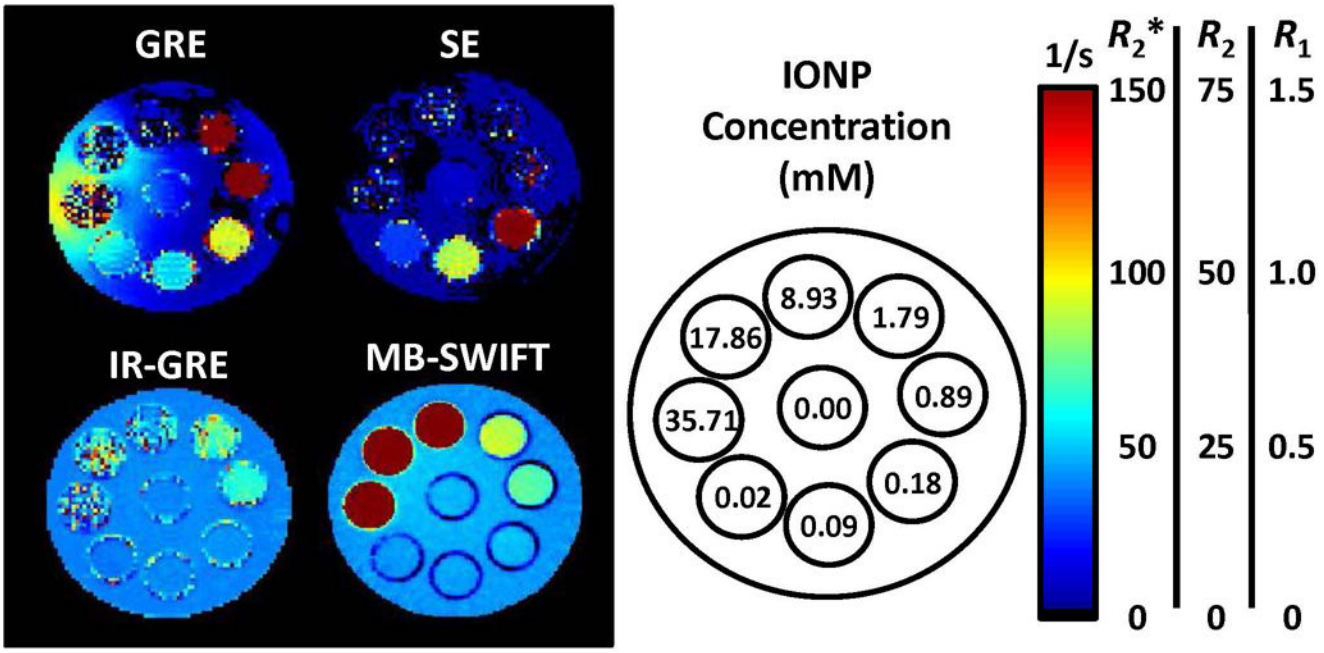

Figure 1.

Comparison of relaxation rate maps for each of the pulse sequences. Within the GRE image, the impact of field inhomogeneity on the background saline of the phantom which is caused by the presence of IONPs is noticeable around the 35.71 mM sample. Additionally, the highest concentrations measured (> 8.93 mM) cannot be quantified with GRE. SE was observed to have a lower dynamic range than GRE. IR-GRE obtains similar measurements to SWIFT, however, the T_2 and T_2* effects impact the signal at higher IONP concentrations. SWIFT was able to detect the entire range imaged (0.02 to 35.71 mM).

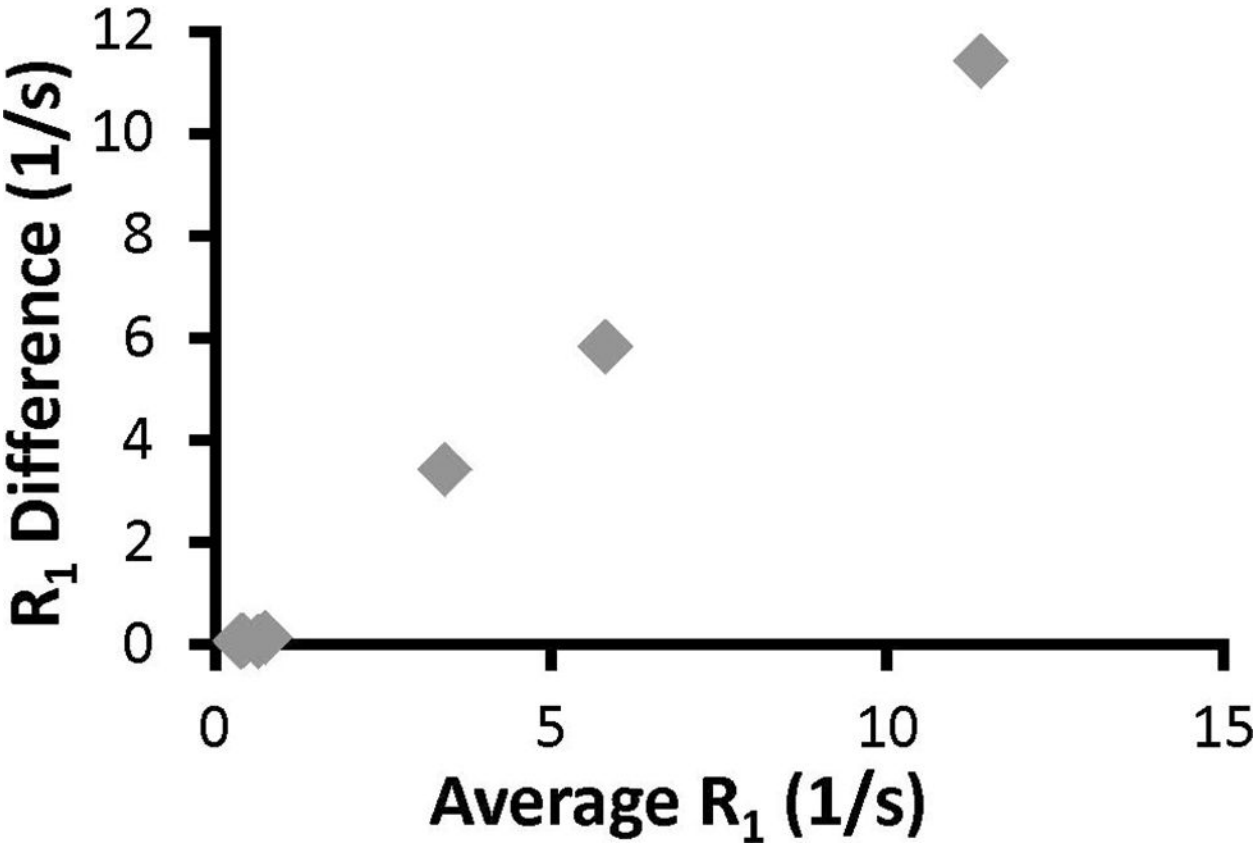

Figure 2.

A Bland-Altman plot comparing the gold-standard IR-GRE to SWIFT. The Bland-Altman plot demonstrates the difference between the measurement methods (y-axis) as a function of the changing R_1 value (x-axis). If the two methods were identical, all points should be on the x-axis. IR-GRE is susceptible to T_2 and T_2* effects at high IONP concentrations, therefore, deviation between the two methods becomes noticeable at average R_1 = 0.65 1/s (0.89 mM).

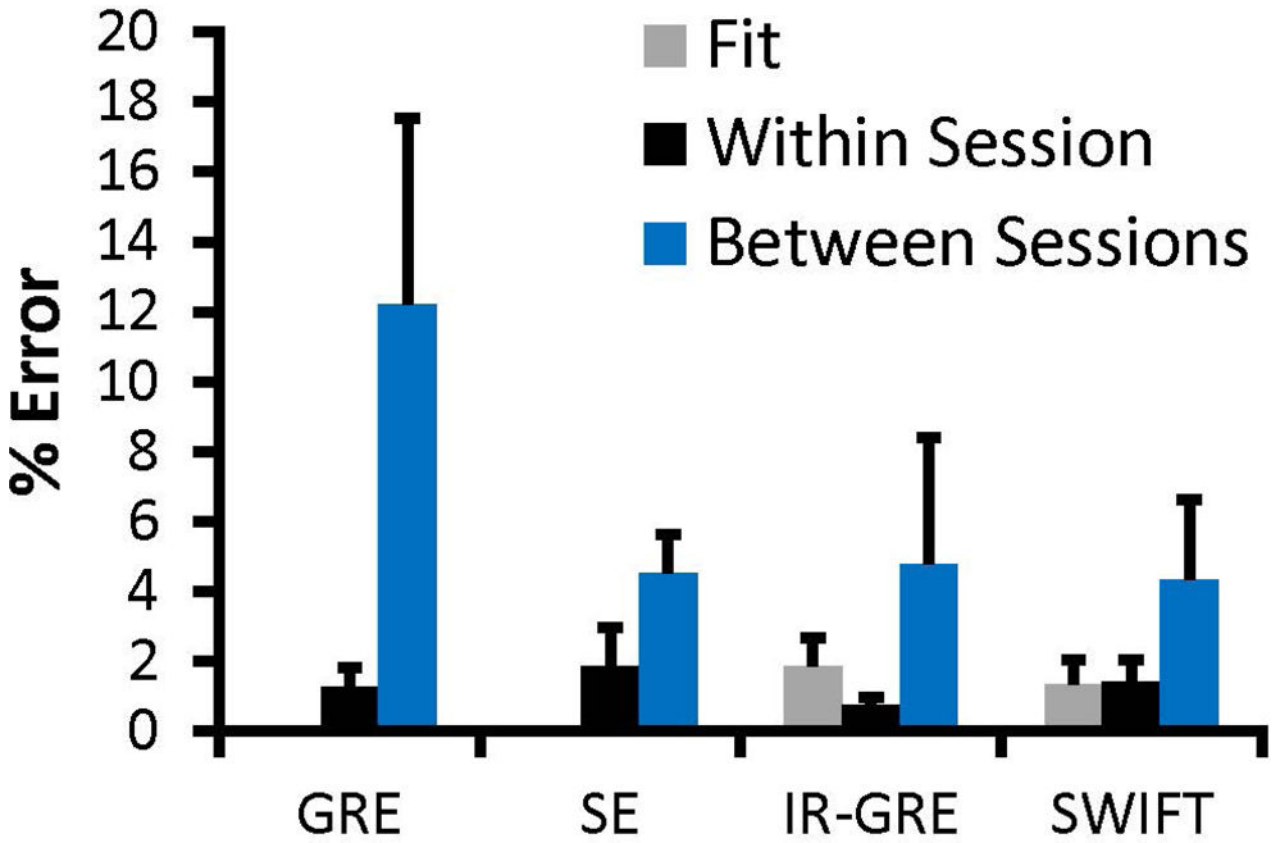

Figure 3.

R_x Error comparison. This error comparison shows the different sources of R_x error as a percentage of the R_x value. The error bars indicate the standard deviation of that percentage error across the detectable range. GRE, IR-GRE, and SWIFT were evaluated across the 0 – 1.79 mM dynamic range (n = 6), whereas SE is evaluated across its shortened dynamic range (0 – 0.18 mM; n = 4). “Fit” indicates the standard error due to the exponential fit. “Within Session” indicates the standard deviation across images acquired within the same session. “Between Sessions” indicates the standard deviation across during separate imaging sessions. The GRE and SE fit values are 0.00014% and 0.006%, respectively, and are not visible on the current plot.

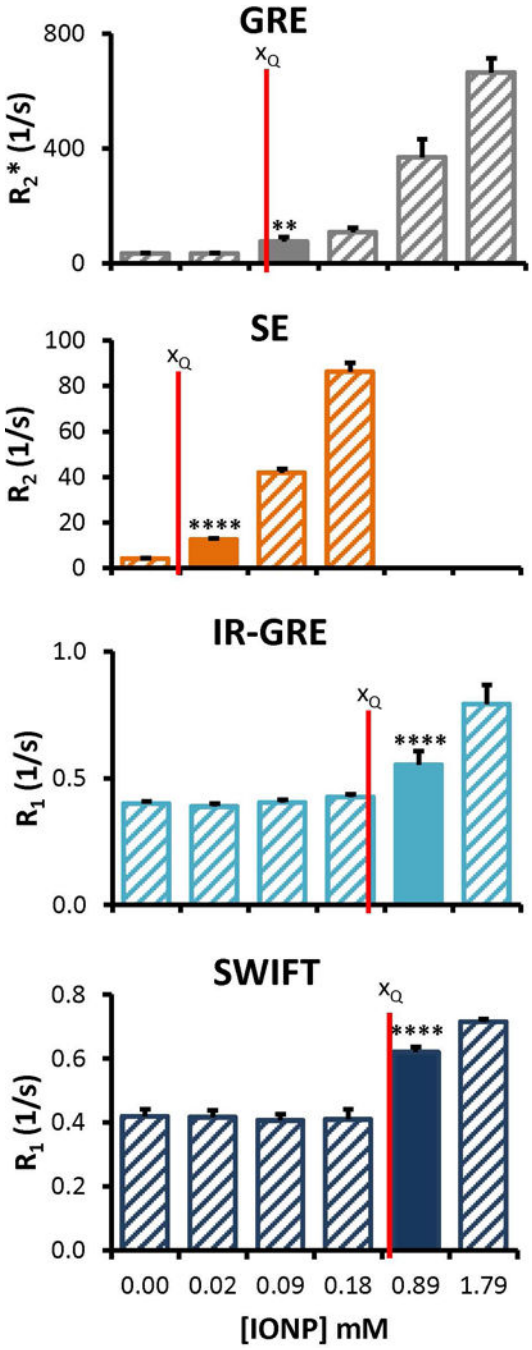

Figure 4.

Comparison of calculated and empirical LOQ. The calculated lower LOQ (x_Q) based on the IUPAC standard (red vertical lines) are compared to the empirically defined limits of measurement (filled columns). The empirically determined minimum is the measured concentration higher than the lower LOQ. Specific values for these plots are available in Table 2. ** $p = 0.001$ to 0.01; **** $p < 0.0001$; p-values are for the comparison with the control, listed in Table 2.

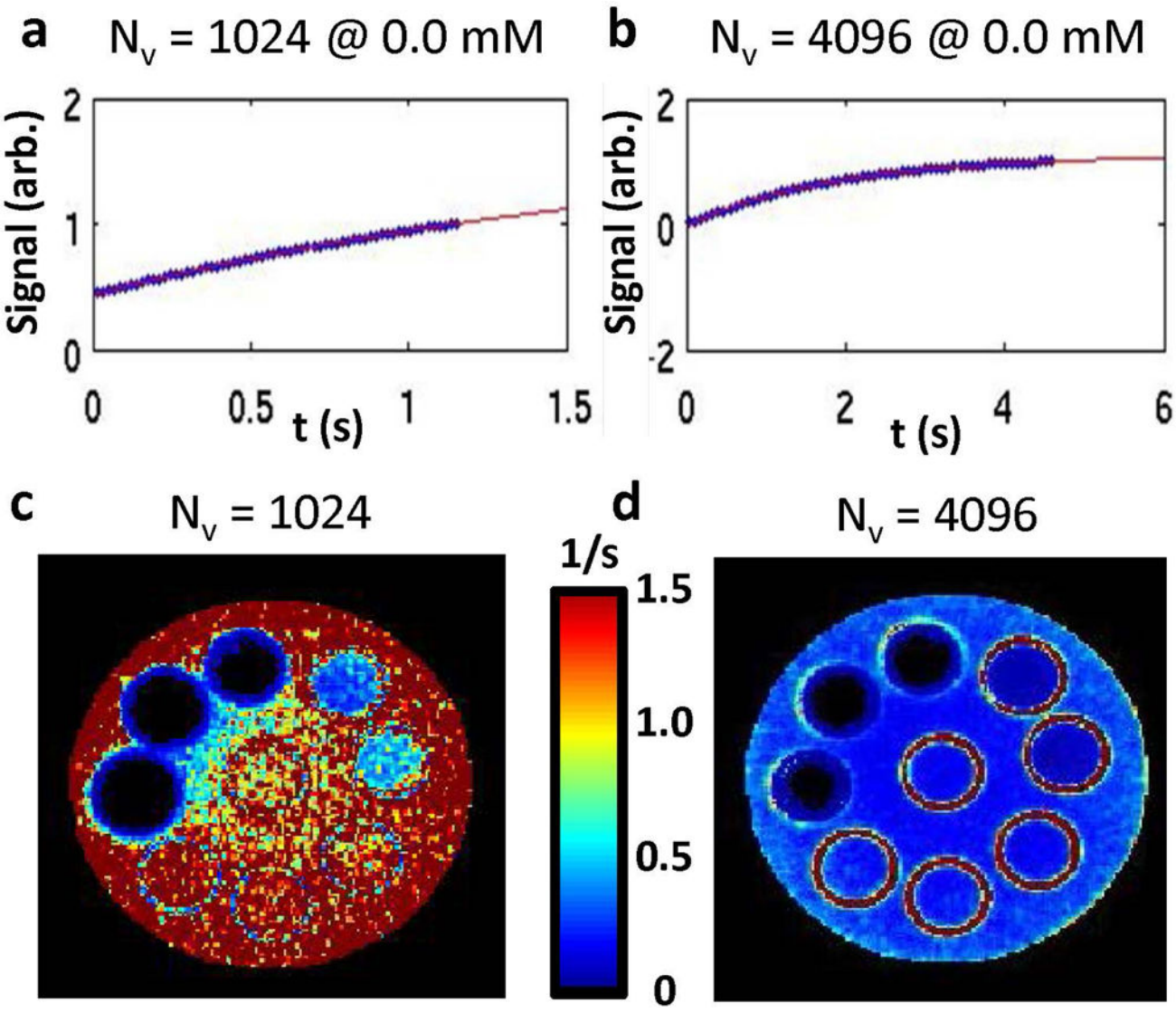

Figure 5.

A comparison is shown between two different SWIFT settings. The time points acquired along the exponential fit for SWIFT are shown with N_v = 1024 (A) and N_v = 4096 (B). The corresponding maps for the exponential fit standard error match the orientation given in Figure 1. The central tubes are 0.00 mM Fe. Starting at the white arrow and going counter clockwise the IONP concentrations increase (0.02, 0.09, 0.18, 0.89, 1.79, 8.93, 17.86, 35.71 mM). The map for N_v = 1024 (C) indicates a high standard fit error compared to N_v = 4096 (D). This indicates that lower IONP concentrations (0.00 – 0.18 mM) should not be determined with the N_v = 1024 settings. Furthermore, both settings are a good fit and show very little standard fit error for the three highest IONP concentrations (8.93 – 35.71 mM).

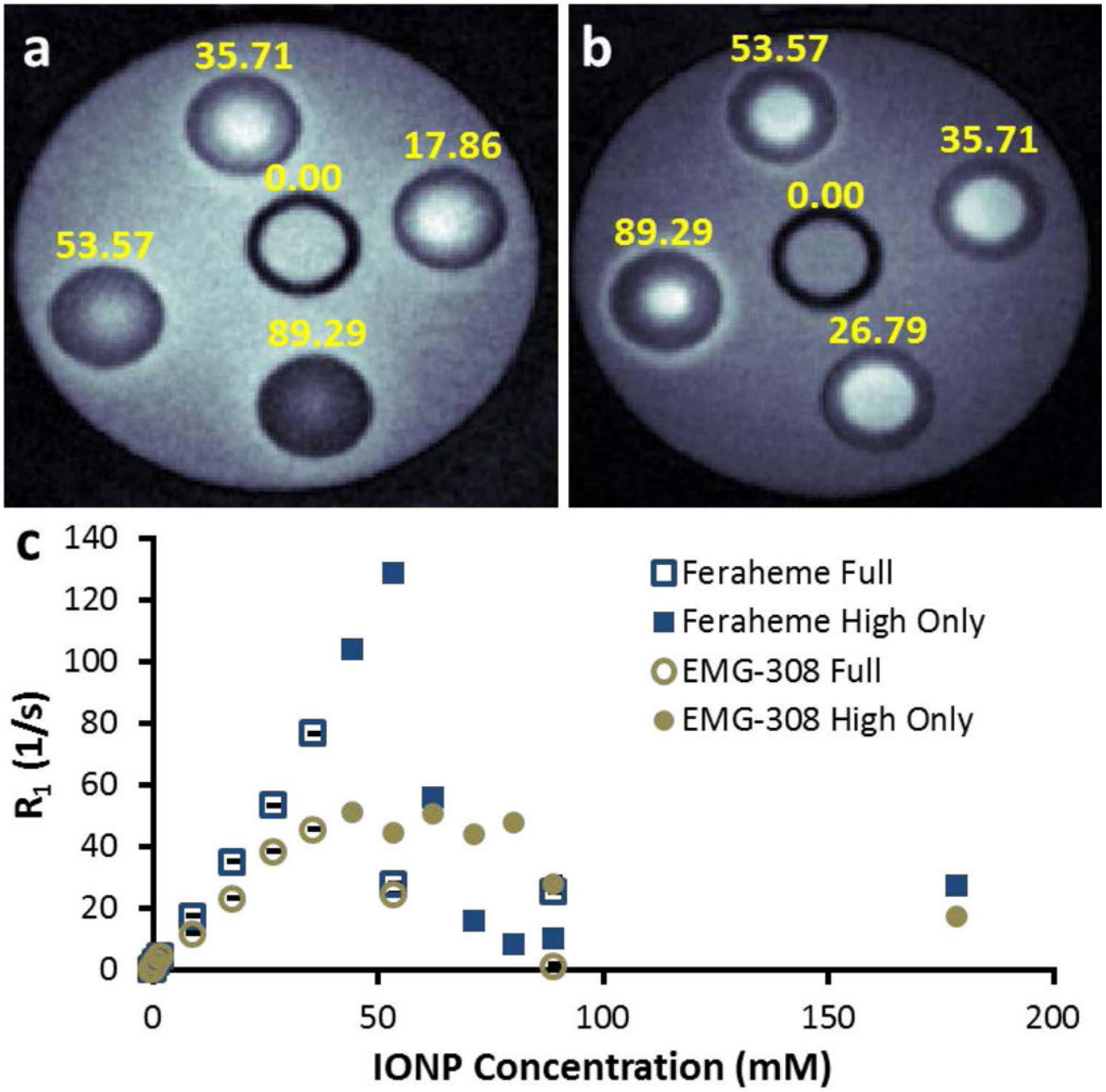

Figure 6.

T_1-weighted SWIFT images show the upper LOQ observable with commercial IONPs: (A) EMG-308 and (B) Feraheme. (C) Quantitative analysis of both images indicates an upper LOQ at 35.71 mM. Two datasets were acquired, “full” indicates an IONP Concentration range from 0 – 89.29 mM; “high only” indicates an IONP Concentration range from 44.64 – 178.57 mM.

Table 1

IUPAC lower limitations

x_C	critical concentration	$x_C = \frac{t_{1-\alpha,\nu} s_0 \eta^{1/2}}{b}$	(Eq. 1)
x_D	limit of detection	$x_D = \frac{(t_{1-\alpha,\nu} + t_{1-\beta,\nu})\, s_0 \eta^{1/2}}{b}$	(Eq. 2)
x_Q	quantification limit	$x_Q = \frac{10 s_0}{b}$	(Eq. 3)
η	function of the ordinary least squares regression parameters	$\eta = \left(\frac{1}{K} + \frac{1}{I} + \frac{\overline{x}^2}{\sum_{i=1}^{I} (x_i - \overline{x})^2} \right)^{1/2}$	(Eq. 4)
$t_{1-\alpha,\nu}$	Student's t distribution corresponding to (1−α) confidence level and ν degrees of freedom, α and β are assumed to be 0.05 for IUPAC		
s_0	standard deviation of blank		
K	number of measurements performed on the blank sample		
b	calibration slope[$]		
I	number of standard solutions		
$\overline{x}$	mean of I standards	$\overline{x} = \frac{1}{I} \sum_{i=1}^{I} x_i$	(Eq. 5)
x_i	concentration of calibration standard		

[$] The calibration slope is estimated from a least squares regression of signal on concentration of the calibration standard.

Table 2

Calculated vs. Empirical Average Lower Limit of Quantification (LOQ)

msIONP Lower Limitations (mM)					
Sequence	Calculated			Empirical	
	x_C	x_D	x_Q	1-way Anova	
GRE	0.01	0.03	0.07	0.09	p = 0.0054
SE	0.001	0.003	0.01	0.02	p = 0.0001
IR-GRE	0.05	0.11	0.26	0.89	p = 0.0001
SWIFT	0.14	0.29	0.73	0.89	p = 0.0001

Empirical values are the lowest concentration determined to be statistically significant from the blank, with the p-value as shown.

Table 3

IONP MR Characteristics at 9.4T

IONP Characteristics at 9.4T				
		msIONP	**EMG-308**	**Feraheme**
SWIFT r_1 ($mM^{-1}s^{-1}$)	slope ($mM^{-1}s^{-1}$)	0.308 ± 0.003	1.317 ± 0.009	2.08 ± 0.04
	minimum (mM)	0.73	0.17	0.11
	maximum (mM)	-----	35.71	35.71
SE r_2 ($mM^{-1}s^{-1}$)	slope ($mM^{-1}s^{-1}$)	431 ± 10	647 ± 66	124.2 ± 0.2
	minimum (mM)	0.006	0.004	0.020
	maximum (mM)	0.18	0.18	1.79
GRE r_2* ($mM^{-1}s^{-1}$)	slope ($mM^{-1}s^{-1}$)	436 ± 19	653 ± 12	128 ± 1
	minimum (mM)	0.07	0.05	0.24
	maximum (mM)	0.89	0.89	1.79